A theoretical study of surface-to-borehole electromagnetic logging in cased holes

A. M. Augustin*, W. D. Kennedy‡, H. F. Morrison§, and K. H. Lee**

ABSTRACT

A new electromagnetic logging method, in which the source is a horizontal loop coaxial with a cased drill hole and the secondary axial fields are measured at depth within the casing, has been analyzed. The analysis, which is for an idealized model of an infinite pipe in a conductive whole space, has shown that the casing and formation are uncoupled at the low frequencies that would be used in field studies. The field inside the casing may be found by first finding the field in the formation and then using this field as an incident field for the pipe alone. This result permits the formation response to be recovered from the measured field in the borehole by applying a correction for the known properties of the casing. If the casing response cannot be accurately predicted, a separate logging tool employing a higher frequency transmitter could be used to determine the required casing parameters in the vicinity of the receiver.

This logging technique shows excellent sensitivity to changes in formation conductivity, but it is not yet known how well horizontal stratification can be resolved. One of its most promising applications will be in monitoring, through repeated measurements, changes in formation conductivity during production or enhanced recovery operations.

INTRODUCTION

At present, once a borehole is cased, the formation behind the casing is virtually inaccessible to standard borehole logging methods. Although techniques based on gamma-ray and neutron scattering are sometimes useful, frequently they are not interpretable. Even under favorable conditions for interpretation, their radius of investigation is no more than centimeters. Measurements of pressure, flow rate, and saturation made downhole are not directly interpretable for fluid distributions outside the casing. A method with the ability to obtain measurements in the presence of casing, and with a radius of investigation measured in meters or tens to hundreds of meters, would be of considerable value in optimizing hydrocarbon recovery programs.

Standard electromagnetic (EM) logging devices (e.g., 6FF40) operate at frequencies too high for their signal to penetrate conductive casings. For fields to penetrate the casing and energize the formation, the frequency of operation would need to be reduced until the thickness of the metal casing was considerably less than the skin depth in that metal. Unfortunately, the response of the formation at that low frequency would be undetectable with practically realizable instrumentation.

However, large-scale above-ground systems are used to map the conductivity of the earth, and these EM soundings employ low frequencies that should easily penetrate a well casing. In this paper, a technique is introduced for logging cased boreholes using a large-loop transmitter located on the surface and a receiver, or receiver array, lowered into the well on a wireline. With this configuration, low-frequency fields from the distant surface transmitter penetrate the casing with little attenuation but still produce secondary fields from the enclosing formation that are measurable. The relative influence of the physical properties of the casing and of the formation on the axial component of the magnetic field inside the casing has been analyzed, and a method for the determination of the apparent resistivity outside the casing has been developed. The technique is referred to as surface-to-borehole logging. Figure 1 illustrates the geometrical configuration of the source loop and casing.

To study this configuration, an analytical solution for the fields on the axis of an infinite pipe embedded in an infinite

conducting whole space has been developed (see the Appendix). This analytical model is probably too idealized to make accurate quantitative interpretations of real data, but its predictions have been verified experimentally, indicating that a more versatile numerical model capable of incorporating both vertical cylindrical and horizontal planar boundaries would yield useful quantitative predictions. Our analytical results were verified by an experimental study using lengths of pipe in free space. These experiments were also used to study more realistic phenomena, in particular the response when the source loop was located in the plane perpendicular to one end of a finite pipe.

The radial response of a cylindrically layered medium to an EM source on the axis is discussed in the borehole logging literature. EM techniques in the borehole were introduced by Doll (1949), but his analysis of the tool response was based on ad hoc hypotheses which correspond to the case of low conductivity or frequency. More general formulations of the induction response appeared in the early 1960s. Moran and Kunz (1962) treated the case of one cylindrical boundary, and Duesterhoeft and Smith (1962) gave a solution for the case of two cylindrical boundaries. In these formulations, the conductivity of each cylindrical shell varies, but its magnetic permeability is held constant. Anderson (1968) studied the effect of magnetic permability in an infinite medium outside the borehole on the quadrature component of the induction log response. Wait and Hill (1977) analyzed the shielding effect of casing on EM signals generated inside the casing. Hill and Wait (1979) analyzed the EM response of a wire-loop antenna mounted on an infinite conducting pipe for use in

measurement-while-drilling applications. The formulation presented in this paper is similar to that of Duesterhoeft and Smith except, as illustrated in Figure 1, the source is considered to be a finite loop in the x-y plane, centered on the z axis, and embedded in the infinite region outside the cylinders representing the borehole and casing. The effects of variable magnetic permeability in each cylindrical layer are also included. The results presented here are consistent with all the previously published studies but extend the area of application to a new technique for formation evaluation.

Analytical model

The vertical component of magnetic field inside the casing depends upon distance from the axis r, distance from the source plane $|z - z'|$, and angular frequency ω. It is shown in the Appendix that this field can be expressed as

$$H_z(r, z, \omega) = \frac{aI(\omega)}{2\pi} \int_{z'}^{+\infty} \gamma_1 f_1(k_z) I_0(\gamma_1 r) e^{-ik_z|z - z'|} \, dk_z, \qquad (1)$$

where a is the source loop radius, $I(\omega)$ is the current exciting the source, k_z is the wavenumber for the vertically propagating component of the solution, $I_0(\gamma_1 r)$ is the modified Bessel function of the first kind of order zero, $\gamma_1 = \sqrt{k_z^2 - k_1^2}$, and k_1 is the propagation constant in the first shell. The amplitude coefficient $f_1(k_z)$ is a complicated function depending on the physical properties of the casing and surrounding medium, as well as on the transform variable k_z. Equation (1) evaluated at $r = 0$ is the basis for the numerical model used in this study.

SCALE-MODEL EXPERIMENTS

In order to distinguish magnetic from EM effects for verification of the numerical model, measurements were made in two different pipes: a conductive, nonmagnetic copper pipe of 9 m length, 0.063 m inner diameter, and 0.002 m wall thickness and a conductive, magnetic, soft-steel pipe of 9 m length, 0.063 m inner diameter, and 0.0043 m wall thickness. The source loop was eight turns of copper wire on a circular form 0.61 m in radius.

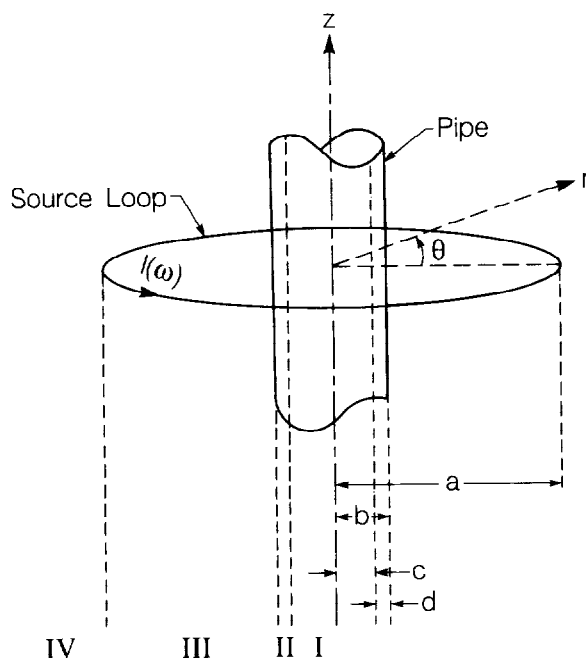The source loop was excited by sine waves on a logarithmic

FIG. 1. Geometrical configuration of the source loop and the casing. A cylindrical coordinate system (r, θ, z) is used. $I(\omega)$ is the current in the source loop; a is the source loop radius; b is the outer radius of the pipe; c is the pipe inner radius; and d the pipe wall thickness. Regions I, II, III, and IV are defined in order to establish the mathematical formulation. The pipe is considered infinite.
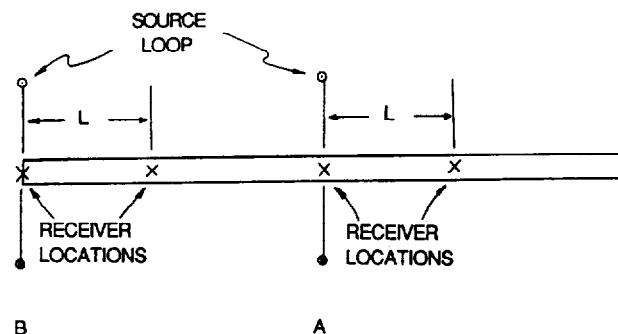
FIG. 2. Relative positions of the pipe, the source loop, and the receiver during the experiment. An infinite pipe was modeled by positioning the source loop in the midplane of the pipe, as indicated by A. A semiinfinite pipe was modeled by positioning the source loop in the endplane of the pipe, indicated by B. $L = 1.49$ m.

frequency interval from 0.06 Hz to 3000 Hz. The waves were generated by a Wavetec Model 171 signal generator and amplified using a Crown Laboratory Amplifier-M 600. The axial component of the magnetic field was measured with a Develco 9200C fluxgate magnetometer (500 Hz bandwidth). The signals were analyzed on a Hewlett Packard Spectrum Analyzer, model 3582A; for the measurements at dc, a Hewlett Packard Multimeter, model 3457A (7 digits), was used.

The two pipe configurations adopted for the experiment are illustrated in Figure 2 Configuration A shows a simulated infinite pipe corresponding to the analytical model. The source loop was centered on the midplane of the pipe, and the magnetic field was recorded on the axis of the pipe at distances 0.0 m and 1.49 m from the plane of the source loop. In the second configuration, B, the source loop was positioned at one end of the pipe simulating a semiinfinite pipe. Measurements were recorded in the plane of the source loop and at 1.49 m from the plane of the source loop.

Experimental results

The experimental results are summarized in Figure 3. Field strength ratio (FSR), the ratio of the absolute value of the magnetic field inside the pipe to the magnetic field at the same point with no pipe present, is plotted as a function of frequency. The rise in FSR for $L = 1.49$ m at higher frequencies is attributed to instrument error and poor calibration of the fluxgate sensor. The cause of the slight separation of the curves at the 1.49 m distance is not known, but may have been caused by errors in magnetometer positioning. The experimental error is estimated to have been less than 10 percent.

At low frequencies, the field inside the copper pipe is the same as in free space; there is no static shielding effect due to the conductive, nonmagnetic pipe. As the frequency increases, the magnetic field inside the pipe is attenuated by the conductive material of the pipe wall; and the FSR decreases quickly. Results are similar in the case of the semiinfinite configuration, except that the rate of decrease of the magnetic field with frequency is less than in the infinite configuration.

The conductive, permeable, iron pipe gives rise to a more complex response. For measurements in the plane of the source loop in the simulated infinite pipe, iron produces a static shielding effect at zero frequency. With increasing frequency, the magnetic field inside the pipe vanishes because of skin effect. Curiously, the static shielding effect is larger in the truncated pipe than in the infinite pipe. As in copper pipe, the rate of decrease of the FSR with increasing frequency is smaller in the truncated iron pipe than in the infinite pipe.

At a distance of 1.49 m from the plane of the source loop, the low-frequency response of the axial component of the magnetic field inside the iron pipe is larger than if the pipe were absent; i.e., FSR > 1. The magnetic field is nearly uniform along the pipe and attenuates less rapidly with distance than the field in free space. Consequently, systematic FSR measurements show a transition from a static shielding effect near the plane of the loop to a static enhancement effect for distances greater than 0.80 m from the plane of the source loop. The enhancement effect persists along the axis for many source radii. As in the previous cases, the skin effect eventually dominates the response at higher frequencies, and the magnetic field vanishes inside the casing. Numerical studies indicate that the magnitude of the static enhancement effect varies inversely with source loop radius.

The effectiveness of the iron pipe in shielding its interior region can be correlated to the geometrical properties of the field. The iron pipe exhibits shielding effects for the static magnetic field when there is appreciable curvature of the imposed field at the surface of the pipe. As the frequency increases, EM induction contributes more shielding. Out of the plane of the source, the static magnetic induction tends to keep the field in the pipe constant, yielding an enhancement in the FSR. At larger distances from the source or if the source radius becomes large, the field is effectively uniform and parallel to the pipe so that the magnetic shielding should vanish. The numerical investigation of these effects in the infinite pipe, discussed in the next section, confirms this last conclusion. Why the truncated pipe is more effective at shielding static and low-frequency fields than the infinite pipe has not been analyzed, but since a practical implementation of this scheme would require a larger transmitter loop, the effect would probably be insignificant.
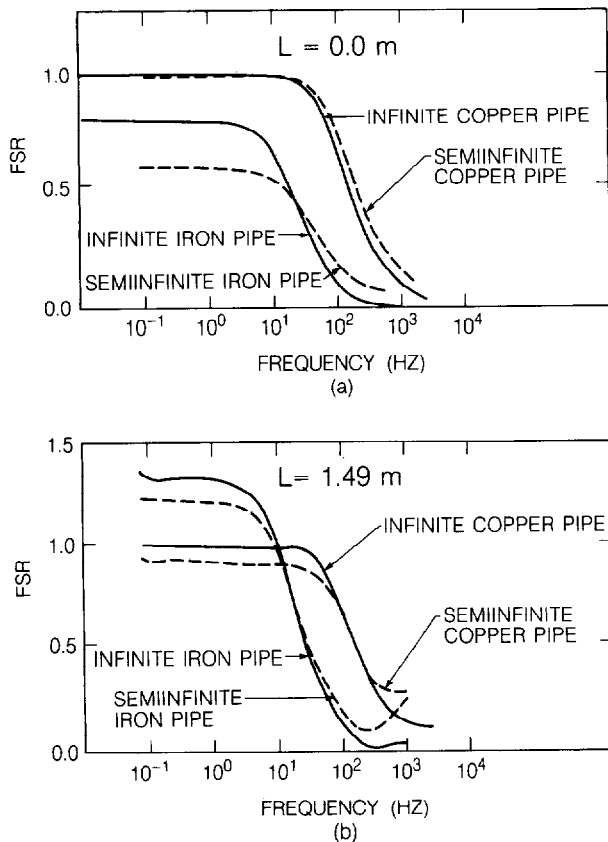

FIG. 3. Field strength ratio FSR (ratio of the magnetic induction at a point inside the pipe to the magnetic induction at the same point with no pipe) versus frequency. Both infinite and semiinfinite cases were simulated using copper tubing and steel casing. (a) Results for the receiver located in the plane of the source loop. (b) Results for the receiver located at 1.49 m from the plane of the source loop.

NUMERICAL MODELING

Test case

The experimental results were compared to the predictions of the numerical model. The conductivity of the copper pipe was estimated to be 3.5×10^7 S/m and its relative magnetic permeability was assigned a value of 1. The conductivity and relative magnetic permeability of the iron pipe were estimated as 8.0×10^6 S/m and 150, respectively, although a magnetic permeability of 50–70 may be more representative of actual casings. Figure 4 shows good agreement between the experimental data and the predictions of the numerical model. This agreement suggests that the numerical model will have acceptable accuracy when applied to simulated field-scale problems.

The numerical model was used to analyze the static mag-

netic enhancement effect seen in the laboratory results. Figure 5 shows the effect of a, the source loop radius, on FSR for two representative frequencies, 0.1 Hz and 10 Hz, with a separation of 1.49 m between the plane of the source loop and the receivers. As a increases, the static enhancement of the field inside the pipe decreases to a frequency-dependent asymptotic value. In free space the static enhancement effect becomes negligible when the ratio of the loop radius to the borehole radius equals about 50 (for the simulated case, $a \sim 3.1$ m).

Simulation of full-scale cases

Although the relative dimensions of the source loop and pipe used in the laboratory experiment were very different from those that would be used in the field, the agreement between their respective results inspired confidence that the predictions of the numerical model would be valid in the field. Accordingly, several numerical models were constructed to study the influence of the casing parameters and formation conductivity on the axial component of the magnetic field inside the standard casing. The fluid filling the casing was assigned a conductivity of 0.5 S/m and a relative magnetic permeability of 1. The radii of the source loop and the borehole were chosen to be 100 m and 0.1 m, respectively, to simulate a typical arrangement envisioned for a full-scale field experiment and to avoid static magnetic enhancement effects. The formation conductivity was first chosen to be zero and its relative magnetic permeability was taken as 1.

In general, the FSR depends upon the physical properties of the three regions in the model, geometrical factors describing the influence of the casing radius and thickness, the source loop radius, source current magnitude and frequency, and the separation between the source loop and the observation point. However, for observation points farther than one source loop radius from the source plane, the FSR becomes practically independent of the distance to the source loop. For a repre-
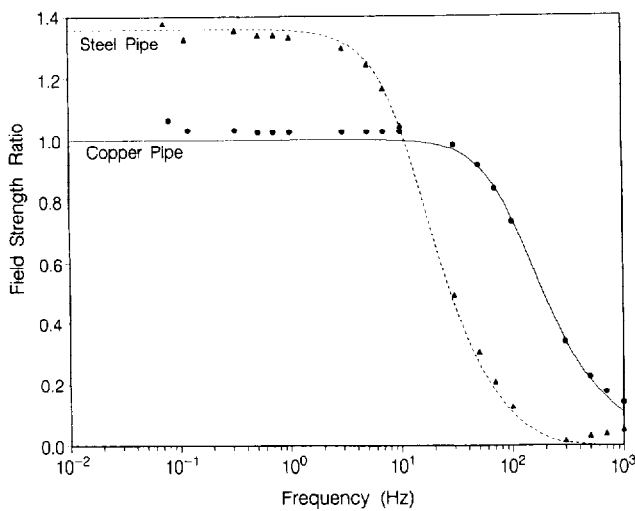

FIG. 4. Comparison between experimental and analytically predicted results. The field strength ratio is the ratio of the axial magnetic field inside the pipe to the axial magnetic field with no pipe. The solid and dashed curves show the theoretical predictions, while the triangles and circles are the experimental results.
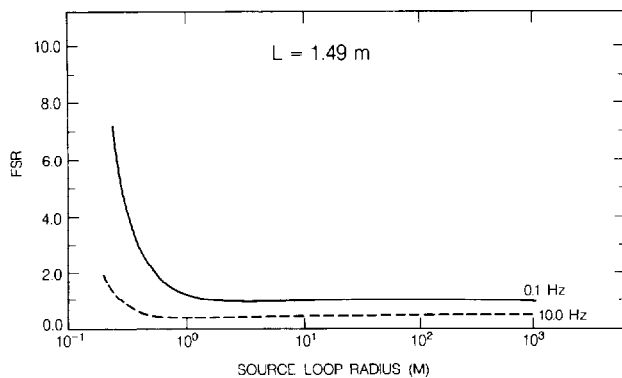

FIG. 5. Influence of the source loop radius on the FSR in free space at two frequencies. The pipe radius is 0.063 m; the thickness is 0.0046 m; the conductivity is 8.0×10^6 S/m; and the relative magnetic permeability is 150. The receiver is located 1.49 m from the plane of the source loop.
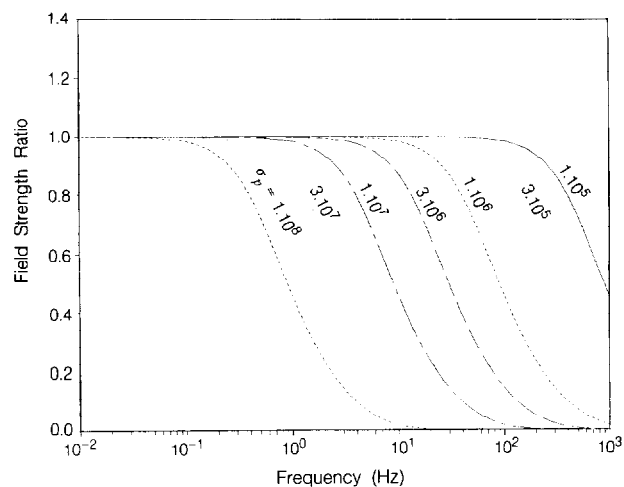

FIG. 6. Influence of the electrical conductivity of the pipe on the field strength ratio versus frequency. The numbers on the curves represent the values of the electrical conductivity of the pipe in S/m. The source loop is of 100.0 m radius; the pipe radius is 0.1 m; the pipe wall thickness is 0.006 m; and the relative magnetic permeability of the pipe is 150.0. The formation has an electrical conductivity of 1.0×10^{-2} S/m and a relative magnetic permeability of 1.0.

sentative separation (i.e., depth) greater than the source loop radius, Figure 6 illustrates the variation of FSR with casing conductivity σ_p, where the subscript p denotes pipe. Virtually the same plot is obtained for any depth greater than one source loop radius. Similar plots result when σ_p is held constant and μ_p, d, or casing radius c is varied. A family of such plots would show that FSR depends upon each of these factors, as would be expected. Generally, the higher the value of these parameters, the lower the frequency at which EM shielding becomes significant. It has been discovered in the analysis of many numerical experiments that the field variations can be simply expressed in terms of an induction parameter, given by $\sigma_p \mu_p d^2 f$, for a pipe of fixed radius.

In order to achieve this simplification, a new quantity is introduced. The normalized secondary field (NSF) is defined as the ratio of the secondary field to the primary, or free-

space, field. The secondary field becomes equal and opposite to the free-space field at high frequencies, so that the total field observed within the casing goes to zero. Thus the NSF is different from the FSR; the latter describes the ratio of the total field to the free-space field. The FSR and NSF are related by FSR $= 1 + $ NSF. The Argand diagram, which plots the real against the imaginary parts of a complex function as a parameter is varied, is useful for analyzing the beahvior of the NSF. Figure 7 is an Argand diagram of the NSF for the casing in free space. The NSF has practically no dependence on receiver position at distances greater than one loop radius from the transmitter and is also practically independent of casing radius: it depends only on the induction parameter.

In Figure 8, for a source loop radius of 100 m, the NSF has been plotted for casing radii of 0.05, 0.1, and 0.2 m, which bracket the radii of common casings. At low and high frequencies, the NSF is independent of casing radius, while in the center spectrum the curves diverge slightly. However, although the NSFs are different for each casing radius, the
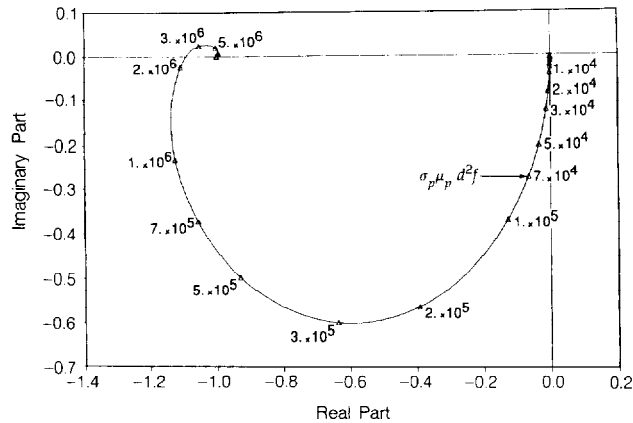

FIG. 7. Argand diagram for the normalized secondary field, NSF, for the casing in free space. The numbers on the curve are the values of the induction parameter $\sigma_p \mu_p d^2 f$, where σ_p is the pipe conductivity, μ_p is its relative magnetic permeability, d is its wall thickness, and f is the frequency. The pipe is 0.0873 m in radius; its wall thickness is 0.0095 m. The electrical conductivity of the pipe is 1.0×10^7 S/m and its relative magnetic permeability is 150.0.

FIG. 9. Argand diagram of the normalized secondary axial magnetic field (NSF) in the formation with no casing (formation response) and in the casing surrounded by the formation (casing-in-formation response). The depth is 100.0 m. The formation and casing conductivities are 1.0×10^{-1} S/m and 1.0 $\times 10^7$ S/m. Their relative magnetic permeabilities are, respectively, 1.0 and 150.0. The source loop has a radius of 100.0 m, while the pipe has a radius of 0.1 m and a wall thickness of 0.006 m.
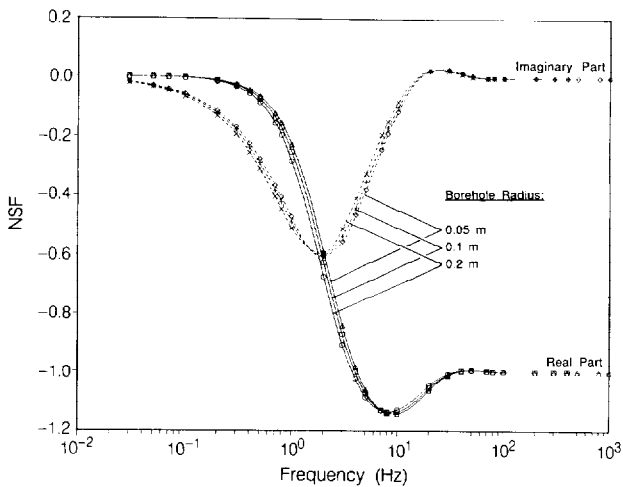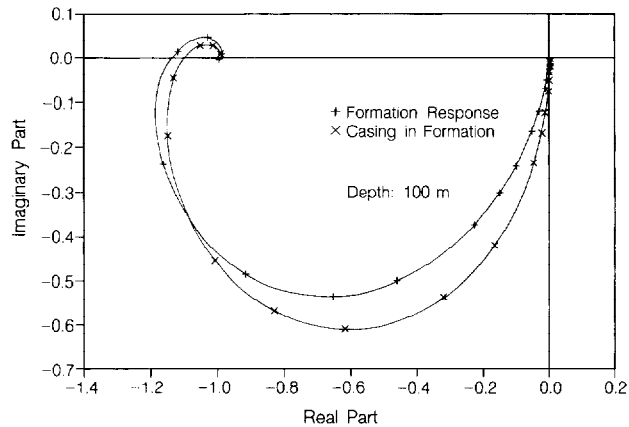

FIG. 8. Influence of the pipe radius on the real and imaginary parts of NSF. The pipe is 0.0095 m thick; its conductivity is 1.0×10^7 S/m; and its relative magnetic permeability is 150.0. The source loop radius is 100. m.
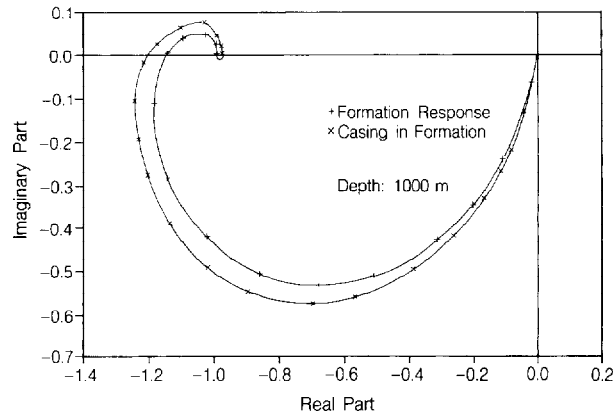

FIG. 10. Same as Figure 9 at a depth of 1000.0 m.

difference is small. In order to simplify the following analyses, the casing radius has been set to 0.0873 m (7 5/8 inch O.D., 35 lb/ft pipe), a typical casing size in oil well drilling and completion.

The NSF is calculated for a receiver in the formation alone (formation response) and for a receiver within the casing (casing-in-formation response) using the algorithm described in the Appendix. The Argand diagrams for the formation response and casing-in-formation response are shown for two depths, 100 m and 1000 m, in Figures 9 and 10. The formation conductivity σ_f in the figures is 0.1 S/m. Note that the formation response lies along the same locus in Figures 9 and 10. This is consistent with the observation that in the formation alone the NSF depends only on the induction parameter $\sigma_f f L^2$, and this dependence is illustrated in Figure 11. Figure 11 would be used to determine an apparent conductivity for the formation, σ_a, in a field experiment without casing in which the real and imaginary parts of the NSF were measured at a given frequency f and depth L.

The Argand diagram for the casing-in-formation response for a depth of 1000 m and a variety of formation conductivities, Figure 12, shows a rather complicated pattern. The curves are well separated, however, and suggest that the formation conductivity could be accurately determined in the presence of casing.

INTERPRETATION METHOD

It was discovered in analyzing these Argand plots that the response of the casing alone and the formation alone could be combined to yield the casing-in-formation response. The total axial magnetic field inside the pipe H^T can be decomposed into

$$H^T = H_f + H_c, \qquad (2)$$

where H_f is the axial magnetic field contributed by the formation in the absence of casing and H_c is the axial magnetic field contributed by the casing. At low frequencies the contribution of the casing to the secondary field in the formation is proportional to the field which would exist at the same point in space with the casing absent. Figure 13 shows that at fixed frequency, $|K| = |H_c/H_f|$ does not, for practical purposes, depend upon the formation conductivity or depth (the variation in the ratio is always in at least the third significant figure). Although absolute values have been plotted for convenience, the real and imaginary parts of the ratio H_c/H_f are independently constant at fixed frequency. Thus

$$H_c = KH_f,$$

where K is a complex constant characteristic of the casing. Therefore

$$H^T = H_f + KH_f,$$

or $\qquad (3)$

$$H^T = (1 + K)H_f.$$

Since in free space $K = H_c/H_f$ and $\sigma = 0$, Figure 13 shows that in the frequency range of interest, K is independent of formation conductivity and depth; it is given by the NSF for the pipe in free space. This result was observed to hold for all frequencies which would be of interest in practical field sur-
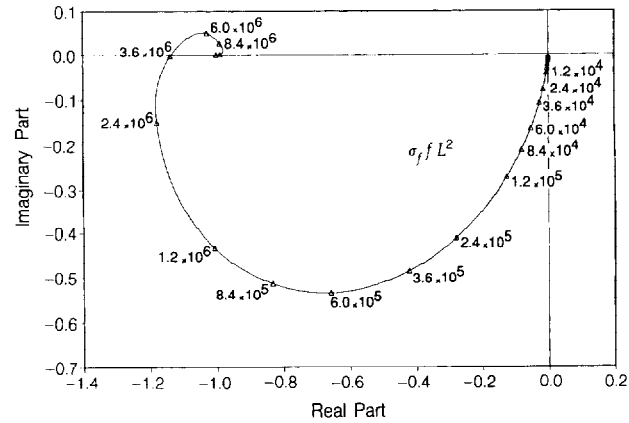

FIG. 11. The normalized secondary axial magnetic field (NSF) due to the formation alone. The numbers on the curve are the values of the factor $L^2 f \sigma_f$, where L is the distance between the transmitter and the receiver, f is the frequency of measurement, and σ_f is the conductivity of the formation.
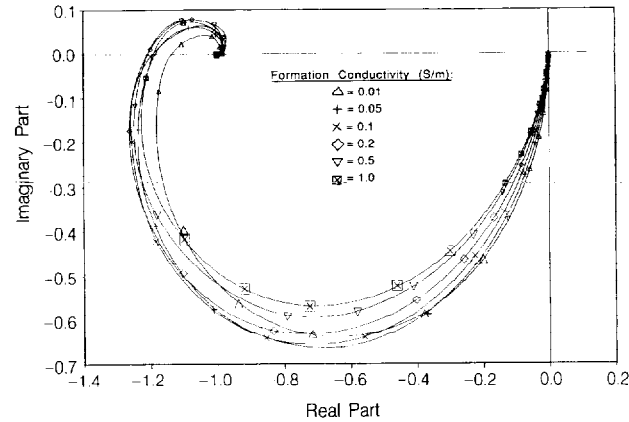

FIG. 12. Argand diagram of the NSF inside the casing surrounded by formations of differing conductivities. The conductivity of the casing is 1.0×10^7 S/m. The relative magnetic permeability of the casing is 150.0. The relative magnetic permeability of the formation is 1.0. The source loop is 100.0 m in radius. The pipe is 0.1 m in radius and has a wall thickness of 0.006 m.

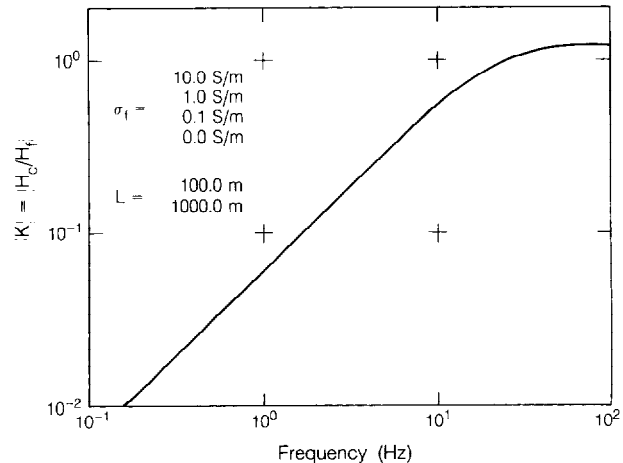FIG. 13. The value of $|K| = |NSF|$ is shown for a source loop radius of 100 m. Altogether this one plot represents eight curves which differ by, at most, about 1 percent. The absolute values are plotted for convenience. In fact, the real and imaginary components of K are separately independent of formation conductivity and observation point. An Argand diagram of K would yield the same curve as shown in Figure 7.

veys. Basically, this result means that the casing is uncoupled from the formation at low frequencies. The field inside (or outside, for that matter) the casing is found by first finding the field that would be present in the formation alone. This field is then considered as a free-space field at the casing and produces a response for the casing as if it were in free space. This field can then be considered a field incident on the casing which induces scattering currents to circulate in the casing as if it were in free space.

Interpretation curve

In a practical survey, the in-phase and the quadrature components of the total axial magnetic field inside the casing $\mathbf{H}^T$ are measured for fixed frequencies. Using the known characteristics of the casing and the frequency, the value of K is equal to the NSF and can be determined using the curve in Figure 7. The field in the formation can then be evaluated using

$$\mathbf{H}_f = \frac{\mathbf{H}^T}{1 + \mathbf{K}}. \tag{4}$$

The field on the axis of a finite loop in free space $\mathbf{H}_p$ corresponding to the survey configuration is given by

$$\mathbf{H}_p = \frac{I}{2} \frac{a^2}{(a^2 + L^2)^{3/2}},$$

where a is the source loop radius, I is the current in the source loop, and L is the separation between the transmitter and the observation point.

Knowing $\mathbf{H}_f$ and $\mathbf{H}_p$, the normalized secondary field due to the formation, $\mathbf{H}_N$, is

$$\mathbf{H}_N = = \frac{\mathbf{H}_f - \mathbf{H}_p}{\mathbf{H}_p}. \tag{5}$$

A single Argand diagram, shown in Figure 11, gives the secondary field in the formation alone as a function of $\sigma_f f L^2$. The value of $\mathbf{H}_N$ derived from equation (5) locates a point on the curve, giving a value of the product $L^2 f \sigma_f$. Since the source-receiver separation L and the frequency f are known, an apparent conductivity σ_a can be determined.

Survey design

The graphs of the FSR versus frequency shown in Figure 6 indicate that the total magnetic field inside a pipe of conductivity greater than $3.0 \times 10^7 \text{S/m}$ vanishes due to the skin effect when frequencies are greater than about 10 Hz. Thus, measurements should be made at frequencies less than 10 Hz.

The skin depth of the formation must also be considered. If possible, the skin depth in the surveyed formation should exceed the depth of the receiver. Frequency can be adjusted to obtain the desired skin depth. For example, to obtain a skin depth of 1000 m in a formation of conductivity 0.1 S/m, the survey frequency of measurement has to be approximately 2 Hz.

Figure 11 suggests the optimum frequency to obtain the maximum resolution of the apparent conductivity. Optimum frequencies are the ones corresponding to the part of the curve were the parameter product values have maximum separation.

Maximum separation occurs when $L^2 f \sigma_f$ is between 7×10^4 and 3×10^6. For a separation of 1000 m and an assumed formation conductivity of 0.1 S/m, the corresponding frequency range is from 0.7 Hz to 30 Hz.

The signal level in boreholes penetrating a conductive, layered half-space has been calculated to vary from 10^{-6} to 10^{-8} gammas per unit moment of source intensity (Morrison et al., 1984). Since relatively large currents and source loops would be used in practical surveys, ample signal would be available for detection at depth using currently available magnetometers.

CONCLUSION

A mathematical formulation for a new surface-to-borehole formation evaluation technique has been developed. Agreement between numerical and scale-model experimental results gives good confidence in the full-scale numerical modeling.

At frequencies for which there is appreciable response from the formation itself, the casing response is of the same order as the formation response and is, moreover, uncoupled from the formation. This means that the casing response can be accurately removed from field measurements and the formation response alone recovered. Knowledge of the casing parameters is required for this process, and it is likely that the practical limits to the resulting formation evaluation will be set by variation in properties of the known casing. Should this be a serious problem, it might be possible to incorporate a second transmitter in the borehole tool which would serve to measure the properties of the casing alone in the vicinity of the receiver. Alternatively, commercially available wireline pipe analysis surveys could be used to estimate casing properties.

This surface-to-borehole logging technique has been analyzed only for a homogeneous whole space. The sensitivity of the method to measurement of formation conductivity through casing is so good that an extension of the analysis to the layered model is warranted and is underway.

One of the most promising abilities of this new logging technique will be to monitor changes in formation conductivity behind casing during production or enhanced recovery processes. In this case the casing response can be presumed to be constant with time and errors in estimating its properties will become second-order errors on the differences in response with time.

REFERENCES

Anderson, W. L., 1968, Theory of borehole magnetic susceptibility measurements with coil pairs: Geophysics, **33**, 962–971.
Doll, H. G., 1949, Introduction to induction logging and application to logging of wells drilled in oil based mud: J. Petr. Tech., **1**, 148–162.
Duesterhoeft, W. C., and Smith, H. W., 1962, Propagation effects on radial response in induction logging: Geophysics, **27**, 463–469.
Hill, D. A., and Wait, J. R., 1979, Calculated admittance of an ideal-

ized drill rod antenna in a lossy medium: Inst. Electr. Electron. Eng. Trans. on Ant. and Prop., **27**, 701–704.

McLachlan, H. W., 1955, Bessel functions for engineers: Oxford Press.

Moran, J. H., and Kunz, K. S., 1962, Basic theory of induction logging and application to two coil sondes: Geophysics, **27**, 829–858.

Morrison, H. F., Phillips, R. J., and O'Brien, D. P., 1969, Quantitative interpretation of transient electromagnetic fields over a layered half space: Geophys. Prosp., **17**, 82–101.

Morrison, H. F., Lee, K. H., and Kennedy, D., 1984, Low frequency electromagnetic logging: 54th Ann. Internat. Mtg., Soc. Explor. Geophys., Expanded Abstracts, 340–343.

Ryu, J., Morrison, H. F., and Ward, S. H., 1970, Electromagnetic fields about a loop source of current: Geophysics, **35**, 862–896.

Wait, J. R., and Hill, D. A., 1977, Electromagnetic shielding of sources within a metal-cased bore hole: Inst. Electr. Electron. Eng. Trans. Geos. Elect., **15**, 108–112.

APPENDIX

MATHEMATICAL SOLUTION

The EM fields due to a finite loop source suspended in air over a layered half-space are given by Morrison et al. (1969) and by Ryu et al. (1970). The EM fields due to a point dipole on the axis of a cylindrically layered medium are obtained by Duesterhoeft and Smith (1962) and Moran and Kunz (1962). Hill and Wait (1979) analyze a wire-loop antenna supported on a conductive drill pipe. There does not seem to have been a previous treatment of the fields of a finite loop on the z axis of a cylindrically symmetrical medium.

In the following treatment, the EM fields for a finite loop source on the axis of an axisymmetric medium are derived. In the problem of immediate concern the loop is embedded in the cylindrically infinite medium farthest from the z axis; however, the formulation used permits a source in any of the cylindrical layers to be modeled by adjustments to components of a single vector representing the source terms.

The electric field **E** and the magnetic field **H** in a linear, isotropic medium are coupled through the Maxwell equations

$$\mathbf{V} \times \mathbf{E} = -\mu \frac{\partial \mathbf{H}}{\partial t} \qquad (A-1)$$

and

$$\mathbf{V} \times \mathbf{H} = \varepsilon \frac{\partial \mathbf{E}}{\partial t} + \mathbf{J}. \qquad (A-2)$$

The current density **J** has a component due to the forcing function and a component due to eddy currents induced in the medium. Thus

$$\mathbf{J} = \mathbf{J}_s + \mathbf{J}_c,$$

where

$$\mathbf{J}_c = \sigma \mathbf{E}.$$

Assuming a time dependence of $e^{j\omega t}$, the forcing function is written

$$\mathbf{J}_s = \frac{a}{r} I(\omega)\delta(r - a)\delta(z - z')\boldsymbol{\theta},$$

where z' locates the plane of the source loop, a is the radius of the loop, and $I(\omega)$ is the frequency-dependent current impressed in the source loop.

Because of the axial symmetry of the problem, the fields have the cylindrical components

$$\mathbf{J} = \mathbf{J}(0, J_\theta, 0),$$

$$\mathbf{E} = \mathbf{E}(0, E_\theta, 0),$$

and

$$\mathbf{H} = \mathbf{H}(H_r, 0, H_z).$$

Application of the curl operator in cylindrical coordinates in equations (A-1) and (A-2) gives

$$\frac{\partial E_\theta}{\partial z} = j\omega\mu H_r, \qquad (A-3)$$

$$\frac{1}{r} \frac{\partial}{\partial r} (rE_\theta) = -j\omega\mu H_z, \qquad (A-4)$$

and

$$\frac{\partial H_r}{\partial z} - \frac{\partial H_z}{\partial r} = J_s + (\sigma + j\omega\varepsilon)E_\theta. \qquad (A-5)$$

After elimination of H_r and H_z from equations (A-3), (A-4), and (A-5), E_θ satisfies

$$\left[\frac{\partial^2}{\partial r^2} + \frac{1}{r} \frac{\partial}{\partial r} - \frac{1}{r^2} + k_i^2 + \frac{\partial^2}{\partial z^2} \right] E_\theta = j\omega\mu J_s, \qquad (A-6)$$

where

$$k_i = \sqrt{-j\omega\mu_i(\sigma_i + j\omega\varepsilon_i)}$$

is the propagation constant in the ith cylindrical shell.

Equation (A-6) is homogeneous except at the source location. To obtain a general solution, first a solution to the homogeneous equation is written in each region. In the region containing the source, a term to represent source effects is added to the solution of the homogeneous equation. Finally, application of the boundary conditions on the EM fields determines the form of the arbitrary functions in each region. Once a solution for E_θ is obtained, H_z can be obtained using equation (A-4).

In each region, the field satisfies

$$\left[\frac{\partial^2}{\partial r^2} + \frac{1}{r} \frac{\partial}{\partial r} - \frac{1}{r^2} + k_i + \frac{\partial^2}{\partial z^2} \right] E_\theta(r, z, \omega)$$

$$= j\omega\mu_i \frac{a}{r} I(\omega)\delta(r - a)\delta(z - z'). \qquad (A-7)$$

The homogeneous equation can be solved by separation variables. Assume that $E_\theta(r, z, \omega)$ has the form

$$E_\theta(r, z, \omega) = A(\omega)R(r)Z(z). \qquad (A-8)$$

Substitution of equation (A-8) into the homogeneous form of equation (A-6) and subsequent division by $A(\omega)R(r)Z(z)$ gives

$$\frac{R''}{R} + \frac{1}{r} \frac{R'}{R} - \frac{1}{r^2} + k_i^2 = -\frac{Z''}{Z}. \qquad (A-9)$$

Since the left side is a function of r alone while the right side depends only on z, each side must equal a constant. Choosing

the form of the separation constant as k_z^2, the equation in z is written

$$Z''(z) + k_z^2 Z(z) = 0, \tag{A-10}$$

which is satisfied by

$$Z(z) = e^{\pm jk_z(z-z')},$$

where z' is interpreted as the source coordinate and the separation constant is chosen to have the form of a wavenumber in the z coordinate. The equation in $R(r)$ is

$$R'' + \frac{1}{r} R' - \left[(k_z^2 - k_i^2) + \frac{1}{r^2}\right]R = 0.$$

Defining $\gamma_i^2 = k_z^2 - k_i^2$, this is written

$$R'' + \frac{1}{r} R' - \left(\gamma_i^2 + \frac{1}{r^2}\right)R = 0. \tag{A-11}$$

This is the canonical form for the modified Bessel differential equation of order 1, parameter γ, whose solutions are the modified Bessel functions

$$R(\gamma_i r) = f_i^- I_1(\gamma_i r) + f_i^+ K_1(\gamma_i r),$$

(McLachlan, 1955, p. 117), where f_i^- and f_i^+ may depend upon k_z. The solution assumed in equation (A-7) has the form

$$E_\theta(r, z, \omega) = [f_i^- I_1(\gamma_i r) + f_i^+ K_1(\gamma_i r)]e^{\pm jk_z(z-z')}.$$

Because E_θ is satisfied for any k_z, a general solution includes all possible values of k_z, or

$$E_\theta(r, z, \omega) = \int_{-\infty}^{+\infty} [f_i^- I_1(\gamma_i r) + f_i^+ K_1(\gamma_i r)]e^{\pm jk_z(z-z')}\, dk_z.$$

$$\tag{A-12}$$

The sign of the exponential is chosen such that $\mathrm{Re}\,[\pm jk_z(z - z')]$ is negative, since E_θ must decrease as distance from the source increases.

At the source location, separation of variables fails and integral transform methods must be applied. The Fourier transform pair

$$E_\theta(r, z, \omega) \leftrightarrow E_\theta(r, k_z, \omega)$$

and the Hankel transform pair of order n given by

$$H_n\left\{E_\theta(r)\right\} = \int_0^\infty E_\theta(r)r J_n(\lambda r)\, dr = E_\theta(\lambda)$$

and

$$H_n^{-1}\left\{E_\theta(\lambda)\right\} = \int_0^\infty E_\theta(\lambda)\lambda J_n(\lambda r)\, d\lambda = E_\theta(r)$$

are invoked in the solution. Equation (A-7) is written as

$$\left[\frac{\partial^2}{\partial r^2} + \frac{1}{r}\frac{\partial}{\partial r} - \frac{1}{r^2} + k_i^2 + \frac{\partial^2}{\partial z^2}\right]E_\theta(r, z, \omega)$$

$$= j\omega\mu_i \frac{a}{r} I(\omega)\delta(a - r)\delta(z - z'). \tag{A-13}$$

Application of the Fourier transform gives

$$\left[\frac{\partial^2}{\partial r^2} + \frac{1}{r}\frac{\partial}{\partial r} - \frac{1}{r^2} + k_i^2 - k_z^2\right]E_\theta(r, k_z, \omega)$$

$$= j\omega\mu_i \frac{a}{r} I(\omega)\delta(a - r)e^{jk_z z'}.$$

Application of the Hankel transform of order 1 is suggested by the order of equation (A-11). This yields

$$[-\lambda^2 + k_i^2 - k_z^2]E_\theta(\lambda, k_z, \omega) = j\omega\mu_i\, aI(\omega)J_1(\lambda a)e^{jk_z z'}.$$

This equation is solved algebraically for E_θ, resulting in

$$E_\theta(\lambda, k_z, \omega) = -\frac{j\omega\mu aI(\omega)}{\lambda^2 + \gamma^2} J_1(\lambda a)e^{jk_z z'}.$$

Applying the inverse Hankel transform of order 1 to E_θ yields

$$E_\theta(r, k_z, \omega) = -j\omega\mu aI(\omega)\int_0^\infty \frac{J_1(\lambda a)J_1(\lambda r)}{\lambda^2 + \gamma^2}\lambda\, d\lambda\; e^{jk_z z'}.$$

The integral is analytic. Substitution of its value gives

$$E_\theta(r, k_z, \omega) = -j\omega\mu aI(\omega)e^{jk_z z'}\begin{cases} I_1(\gamma_i^2 r)K_1(\gamma_i^2 a); & r < a \\ I_1(\gamma_i^2 a)K_1(\gamma_i^2 r), & r > a \end{cases},$$

$$\mathrm{Re}\,(\gamma^2) > 0.$$

Finally, inverse Fourier transformation gives E_θ

$$E_\theta(r, z, \omega) = -\frac{j\omega\mu aI(\omega)}{2\pi}$$

$$\times \int_{-\infty}^{+\infty}\begin{cases} I_1(\gamma_i^2 r)K_1(\gamma_i^2 a)e^{-jk_z(z-z')}\, dk_z, & r < a \\ I_1(\gamma_i^2 a)K_1(\gamma_i^2 r)e^{-jk_z(z-z')}\, dk_z, & r > a \end{cases}. \tag{A-14}$$

Equation (A-14) has a form suitable for matching to equation (A-12) at the cylindrical boundaries.

In k_z space the total electric field in each region is expressed by

$$E_{\theta_1}(r, k_z, \omega) = -j\omega\mu_1\, aI(\omega)e^{jk_z z'}I_1(\gamma_1 r)f_1(k_z), \tag{A-15}$$

$$E_{\theta_2}(r, k_z, \omega) = -j\omega\mu_2\, aI(\omega)e^{jk_z z'}$$

$$\times [I_1(\gamma_2 r)f_2^-(k_z) + K_1(\gamma_2 r)f_2^+(k_z)], \tag{A-16}$$

$$E_{\theta_3}(r, k_z, \omega) = -j\omega\mu_3\, aI(\omega)e^{jk_z z'}$$

$$\times [K_1(\gamma_3 r)f_3(k_z) + I_1(\gamma_3 r)K_1(\gamma_3 a)], \tag{A-17}$$

and

$$E_{\theta_4}(r, k_z, \omega) = -j\omega\mu_3\, aI(\omega)e^{jk_z z'}$$

$$\times [K_1(\gamma_3 r)f_3(k_z) + I_1(\gamma_3 a)K_1(\gamma_3 r)], \tag{A-18}$$

where I_0, I_1, K_0, and K_1 are the modified Bessel functions of the first and second kinds of order 0 and 1 and f_1, f_2^-, f_2^+, and f_3 are unknown coefficients. Using the relation between H_z and E_θ in equation (A-4), the vertical magnetic field in each region is expressed by

$$H_{z_1}(r, k_z, \omega) = aI(\omega)e^{jk_z z'}\gamma_1 f_1(k_z)I_0(\gamma_1 r), \tag{A-19}$$

$$H_{z_2}(r, k_z, \omega) = aI(\omega)e^{jk_z z'}\gamma_2$$

$$\times [f_2^-(k_z)I_0(\gamma_2 r) - f_2^+(k_z)K_0(\gamma_2 r)], \tag{A-20}$$

and

$H_{z_3}(r, k_z, \omega) = aI(\omega)e^{jk_z z'}\gamma_3$

$$\times \; [K_1(\gamma_3 a)I_0(\gamma_3 r) - f_3(k_z)K_0(\gamma_3 r)]. \quad (A\text{-}21)$$

The boundaries divide the space into four coaxial cylindrical regions. Figure 1 illustrates that in regions I and II, only a secondary field (no source term) exists, while in regions III and IV, both a primary field (due to the source loop) and a secondary field (due to the eddy currents in the medium) exist. At the boundaries between regions I and II and between regions II and III, H_z and E_θ are continuous. Application of the boundary conditions yields the system of equations

$\mu_1 I_1(\gamma_1 b)f_1(k_z)$

$$= \mu_2[I_1(\gamma_2 b)f_2^-(k_z) + K_1(\gamma_2 b)f_2^+(k_z)], \quad (A\text{-}22)$$

$\gamma_1 I_0(\gamma_1 b)f_1(k_z)$

$$= \gamma_2[I_0(\gamma_2 b)f_2^-(k_z) - K_0(\gamma_2 b)f_2^+(k_z)], \quad (A\text{-}23)$$

$\mu_2[I_1(\gamma_2 d)f_2^-(K_z) + K_1(\gamma_2 d)f_2^+(K_z)]$

$$= \mu_3[K_1(\gamma_3 d)f_3(K_z) + I_1(\gamma_3 d)K_1(\gamma_3 a)], \quad (A\text{-}24)$$

and

$\gamma_2[I_0(\gamma_2 d)f_2^-(k_z) - K_0(\gamma_2 d)f_2^+(k_z)]$

$$= \gamma_3[K_1(\gamma_3 a)I_0(\gamma_3 d) - K_0(\gamma_3 d)f_3(k_z)]. \quad (A\text{-}25)$$

These equations are linear in the unknown coefficients, which can be obtained using matrix algebra:

$$
\begin{bmatrix}
\mu_1 I_1(\gamma_1 b) & -\mu_2 I_1(\gamma_2 b) & -\mu_2 K_1(\gamma_2 b) & 0 \\
\gamma_1 I_0(\gamma_1 b) & -\gamma_2 I_0(\gamma_2 b) & \gamma_2 K_0(\gamma_2 b) & 0 \\
0 & \mu_2 I_1(\gamma_2 d) & \mu_2 K_1(\gamma_2 d) & -\mu_3 K_1(\gamma_3 d) \\
0 & \gamma_2 I_0(\gamma_2 d) & -\gamma_2 K_0(\gamma_2 d) & \gamma_3 K_0(\gamma_3 a)
\end{bmatrix}
$$

$$
\times
\begin{bmatrix}
f_1 \\ f_2^- \\ f_2^+ \\ f_3
\end{bmatrix}
=
\begin{bmatrix}
0 \\
0 \\
\mu_3 I_1(\gamma_3 d)K_1(\gamma_3 a) \\
\gamma_3 K_1(\gamma_3 a)I_0(\gamma_3 d)
\end{bmatrix}. \quad (A\text{-}26)
$$

When the result for $f_1(k_z)$ is substituted in equation (A-15) and the inverse Fourier transform applied, the expression for the axial magnetic field in region I is obtained:

$$H_{z_1}(r, z, \omega) = \frac{aI(\omega)}{2\pi} \int_{-\infty}^{+\infty} \gamma_1 f_1(k_z)I_0(\gamma_1 r)e^{-jk_z(z-z')} \, dk_z.$$

$$(A\text{-}27)$$

Equation (A-27) evaluated at $r = 0$ is the basis for the numerical model used in this study.